Quantum Feature Space of a Qubit Coupled to an Arbitrary Bath

Chris Wise[1,*], Akram Youssry[2], Alberto Peruzzo[2,3], Jo Plested[1], and Matt Woolley[4]

[1]School of Systems and Computing, UNSW, Canberra, ACT, 2601, Australia

[2]Quantum Photonics Laboratory and Centre for Quantum Computation and Communication Technology, RMIT University, Melbourne, VIC 3000, Australia

[3]Quandela, Massy, France

[4]School of Engineering and Technology and Centre for Engineered Quantum Systems, UNSW, Canberra, ACT, 2601, Australia

*Author to whom any correspondence should be addressed.

E-mail: `c.wise@unswalumni.com`

Abstract. Qubit control protocols have traditionally leveraged a characterisation of the qubit-bath coupling via its power spectral density. Previous work proposed the inference of noise operators that characterise the influence of a classical bath using a grey-box approach that combines deep neural networks with physics-encoded layers. This overall structure is complex and poses challenges in scaling and real-time operations. Here, we show that no expensive neural networks are needed and that this noise operator description admits an efficient parameterisation. We refer to the resulting parameter space as the *quantum feature space* of the qubit dynamics resulting from the coupled bath. We show that the Euclidean distance defined over the quantum feature space provides an effective method for classifying noise processes in the presence of a given set of controls. Using the quantum feature space as the input space for a simple machine learning algorithm (random forest, in this case), we demonstrate that it can effectively classify the stationarity and the broad class of noise processes perturbing a qubit. Finally, we explore how control pulse parameters map to the quantum feature space.

Keywords: quantum control, quantum features, classification, clustering

1. Introduction

Noise in quantum computers that results in qubits losing coherence (decoherence) is due to unwanted bath coupling [1]. One way to mitigate decoherence is to decouple the qubit from the bath by applying a control field as a series of pulses [2]. This technique was first studied in nuclear magnetic resonance imaging [3, 4]. Within this framework, control pulses are applied for a time τ and then turned off for a time τ, and this pattern is repeated N times. This oscillating pulse sequence design is the Carr-Purcell-Meiboom-Gill (CPMG) sequence [5, 6].

Álvarez and Suter (AS) proposed a modified CPMG sequence to perform qubit spectroscopy [7]. AS pulses are part of a family of pulses used for dynamical decoupling noise spectroscopy, and they can be used to infer qubit coherence as a function of time. These empirical coherence data, obtained by AS pulses, are fitted to theoretical coherence curves corresponding to parametric noise spectra [8, 9]. However, this method requires an accurate model of system dynamics [10], which can be challenging to develop in general [11]. Furthermore, if an inappropriate parametric noise spectrum is chosen *a priori*, the estimated noise spectrum will correspond to an inaccurate model of system dynamics, and subsequently, control pulses optimised using this system model will likely be suboptimal [11].

More direct methods of noise spectroscopy include techniques such as two-point correlation, which measures the correlation function of the noise by implementing gates at different times and measuring the change in the qubit state [12]. The Fourier transform of this correlation function gives the noise spectrum. However, this method can be resource intensive, time-consuming, computationally expensive, and requires that the noise be stationary [8, 10, 13, 14].

The authors of [14] developed a quantum noise spectroscopy method that used the Fourier transform of the measurements of the free-induction decay of the coherence curves. The technique accurately recovered the correct noise spectra and outperformed previous decoupling schemes while significantly reducing experimental overhead. However, the method makes several assumptions that limit the applicability of the work. For example, the authors assume the qubit is only subject to dephasing, where the qubit thermal relaxation process occurs over a much longer time scale than phase randomisation, and that the frequency fluctuations of a qubit are subject to stationary zero-mean Gaussian noise.

In [10], researchers instead used deep learning techniques to infer accurate qubit noise spectra. The method used coherence curves as input to a recurrent neural network with a feedforward neural network head to estimate the noise spectrum. They showed that the model could accurately estimate the qubit noise spectrum using only the coherence curves and outperformed the standard noise spectroscopy techniques. Researchers in [13] further demonstrated the effectiveness of deep learning by using it to reconstruct the

power spectral density (PSD) of an ensemble of carbon impurities around a diamond's nitrogen-vacancy centre.

Youssry et al. [15] introduced a grey-box model separating control and system-bath dynamics. In this work, time-dependent Hamiltonians and unitaries specified the control dynamics, and a form of recurrent neural network (a gated recurrent unit) was used to predict the system-bath dynamics associated with control pulses. The input to this neural network was parameterised control pulses as a sequence of vectors. The model output was the parameterisation of a noise operator. The authors showed that the grey-box model could be used for qubit control pulse optimisation and qubit noise spectroscopy. This grey-box model approach was later used for qubit control in the presence of a non-Markovian bath [16]. The formalism used in this work is discussed in more detail in Sec. 2.

Despite the success of [10, 13, 15, 16], these approaches are limited by their use of deep learning models, specifically the expense of training deep learning models and the need for large datasets. Expensive models are undesirable as noise processes in quantum systems can drift over time [17, 18], necessitating new training data and model retraining potentially daily or even hourly. Additionally, noise profiles may change from one physical qubit to another [19], so a specific model may be required for each qubit, which does not scale. Furthermore, specific to the grey-box method of [15, 16], the white-box aspect (the so-called physics-informed aspect of the network) scales exponentially with the dimensions of the quantum system, adding to the challenge of moving beyond toy problems.

This variability of qubit noise profiles, both in terms of time and between qubits, and the exponential scaling of the grey-box model, motivated the need to move beyond deep learning models for noise spectroscopy and to find feature spaces that can be used to classify qubit noise profiles without deep learning models.

We introduce in this paper *quantum feature spaces*, which encode the bath's influence on system dynamics while making minimal assumptions about the bath such that it can be used beyond toy problems and have utility for a broad range of physically realised qubits. The quantum feature space is deduced from observable expectations using efficient linear regression models. We then show that no expensive algorithms are needed to classify the noise affecting a qubit; instead, we use the Euclidean distance within the quantum feature space for classification. Fig. 1 demonstrates further uses for the quantum feature space. The feature space can be used as the input space to simple machine learning algorithms for noise classification, or the space can enable control pulse optimisation via visualising how control pulse parameters manifest themselves in the quantum feature space.
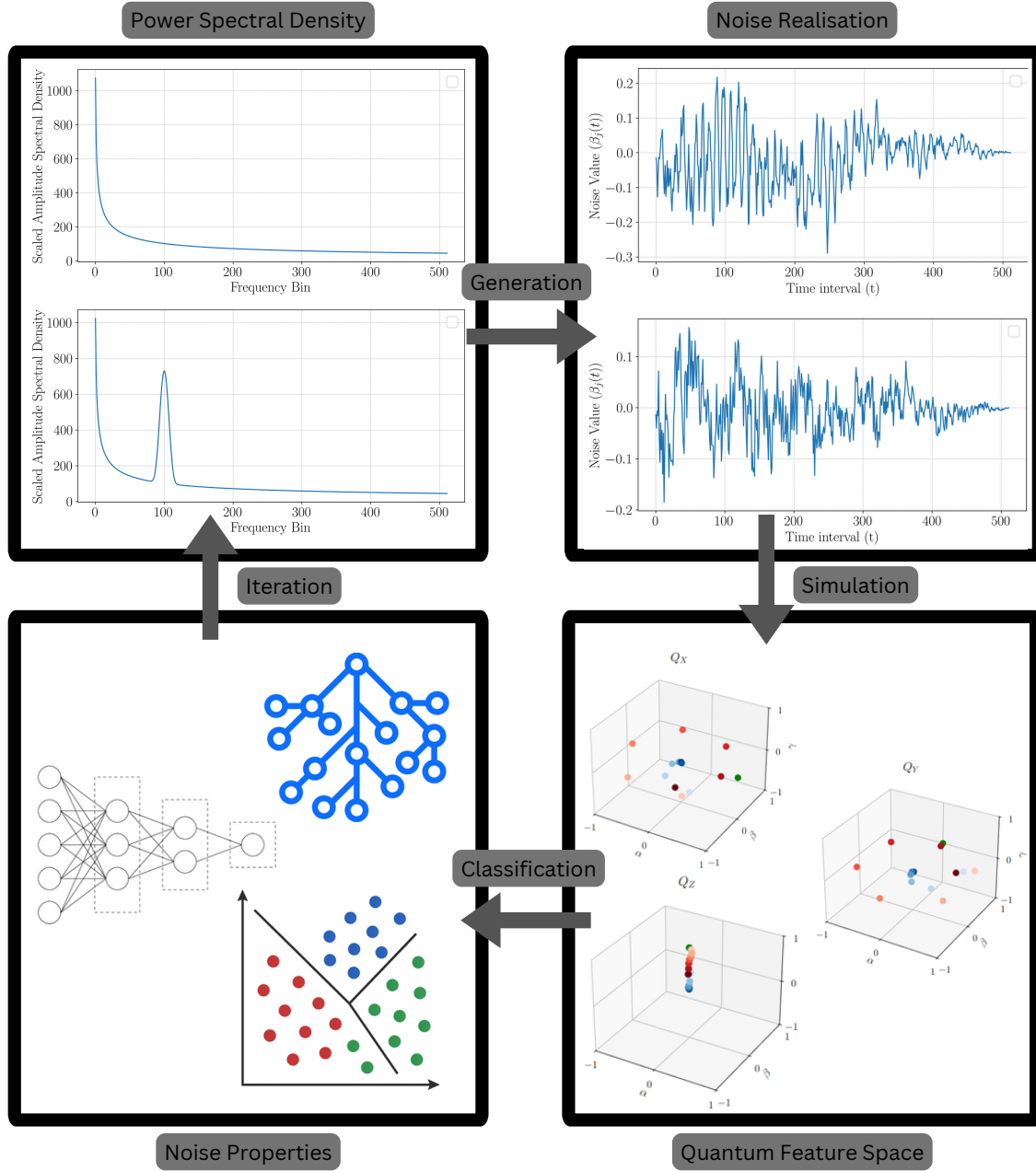
Figure 1: The diagram illustrates an iterative process for characterising and learning noise properties in quantum systems. Starting with a power spectral density (PSD) (top), noise realisations are generated (right) and combined with control pulses in a quantum simulation. The outcomes of these simulations are mapped onto a quantum feature space (bottom), where data points encode the effects of the noise. This feature space is used by regression models such as decision trees to infer key noise properties, including type and stationarity (left). These inferred properties refine the PSD model used in subsequent iterations. This closed-loop framework enables the classification and clustering of noise processes. It facilitates tailored noise mitigation strategies, leveraging machine learning techniques like decision trees, k-means clustering, and neural networks for enhanced quantum control.

2. Theoretical Results

2.1. Open System Dynamics

The Hamiltonian describing a controlled qubit (the system) interacting with a bath is,

$$H(t) = H_{ctrl}(t) + H_{SB}(t) \tag{1}$$

where the control Hamiltonian is,

$$H_{\text{ctrl}}(t) = \Omega \frac{\sigma_z}{2} + \sum_{j=\{x,y,z\}} f_j(t) \frac{\sigma_j}{2} \tag{2}$$

where Ω is the qubit's energy gap and $f_j(t)$ is a control pulse along the given axis, and the system-bath Hamiltonian is,

$$H_{SB}(t) = \sum_{j=x,y,z} \sigma_j \otimes B_j(t) \tag{3}$$

with $B_j(t) = \hat{B}_j(t) + \beta_j(t)I_B$ capturing a quantum bath via the operator $\hat{B}_j(t)$ and classical noise via the stochastic process $\beta_j(t)$.

We are interested in the expected value of a system (qubit) observable O at time T given an initial system (qubit) state ρ, where T represents the total time of the control pulse sequence. This is given by,

$$\mathbb{E}\{O(T)\}_\rho = \left\langle \text{Tr}\left[U(T)\left(\rho \otimes \rho_B\right) U(T)^\dagger O \right] \right\rangle \tag{4}$$

where $U(T) = \mathcal{T} e^{-i \int_0^T H(s)\, ds}$ is the time-ordered exponential of the time-dependent Hamiltonian in Eq. (1), $\langle \cdot \rangle$ denotes classical averaging over realisations of the random processes $\beta_j(t)$, and ρ_B is the initial state of the bath.

We then decompose the total system-bath evolution into a product of system-bath dynamics and control dynamics. To do this, Paz-Silva, Norris, and Lorenza [20] used a so-called *toggling frame*, defined by the time-ordered control unitary,

$$U_{\text{ctrl}}(t) = \mathcal{T} e^{-i \int_0^t H_{\text{ctrl}}(s)\, ds} \tag{5}$$

The system-bath Hamiltonian in this toggling frame is,

$$H_{\text{SB}}^{\text{tog}}(t) = U_{\text{ctrl}}^\dagger(t) H_{\text{SB}}(t) U_{\text{ctrl}}(t) \tag{6}$$

with the associated unitary,

$$U_{\text{SB}}^{\text{tog}}(t) = \mathcal{T} e^{-i \int_0^t H_{\text{SB}}^{\text{tog}}(s)\, ds} \tag{7}$$

It can be shown that,

$$U_{\text{SB}}(t) = U_{\text{ctrl}}(t) U_{\text{SB}}^{\text{tog}}(t) U_{\text{ctrl}}^\dagger(t) \tag{8}$$

which allows us to rewrite Eq. (4) as,

$$\mathbb{E}\{O(T)\}_\rho = \text{Tr}\left[V_O(T)U_{\text{ctrl}}(T)\rho U_{\text{ctrl}}(T)^\dagger O\right] \tag{9}$$

where

$$V_O(T) = \left\langle O^{-1}U_{\text{SB}}^\dagger(T)OU_{\text{SB}}(T)\right\rangle_B \tag{10}$$

with $\langle\cdot\rangle_B = \langle\text{Tr}_B\left[\cdot\rho_B\right]\rangle$ representing classical averaging over the partial trace taken with respect to the bath. Physically, we interpret V_O as a so-called *noise operator* that encodes the influence of the system-bath interaction on qubit dynamics.

2.2. Decomposition of the System-Bath Operator

When our system-bath Hamiltonian consists of only classical noise processes, one can move O^{-1} in Eq. (10), and write,

$$V_O = O^{-1}\left\langle U_{\text{SB}}^\dagger OU_{\text{SB}}\right\rangle \tag{11}$$

where the time arguments T have been omitted for brevity. Before continuing, it is important to note some of the mathematical properties of the V_O operator as they subsequently inform restrictions on its parameterisation. Specifically, $\left\langle U_{\text{SB}}^\dagger OU_{\text{SB}}\right\rangle$ is trace bounded by one, is Hermitian, and has real eigenvalues between -1 and 1 [15].

An efficient parameterisation of V_O is provided by its eigendecomposition. This eigendecomposition contains a diagonal matrix D_O whose entries are real numbers in the interval $[-1, 1]$ and whose sum also lies in the interval $[-1, 1]$, and a general unitary matrix Q. Thus Eq. (11) can be rewritten as

$$V_O = O^{-1}Q_O D_O Q_O^\dagger \tag{12}$$

In the case of a qubit, we start with a factorisation of a general 2×2 unitary operator,

$$Q_O = \begin{bmatrix} e^{i\psi_O} & 0 \\ 0 & e^{-i\psi_O} \end{bmatrix} \begin{bmatrix} \cos\theta_O & \sin\theta_O \\ -\sin\theta_O & \cos\theta_O \end{bmatrix} \begin{bmatrix} e^{i\Delta_O} & 0 \\ 0 & e^{-i\Delta_O} \end{bmatrix} \tag{13}$$

where $\psi_O, \theta_O, \Delta_O \in \mathbb{R}$ and the diagonal matrix D_O of Eq. (12) is constructed as

$$D_O = \begin{bmatrix} \mu_O & 0 \\ 0 & -\mu_O \end{bmatrix} \tag{14}$$

where $\mu_O \in [0, 1]$. The matrix D_O can be generalised to non-unital channels [15], but this paper will focus on unital channels, for which $\Phi(I) = I$ [21]. The restriction to unital channels in this study is motivated by the fact that for many physical qubit implementations, the decoherence timescale ($T2$) is observed to be significantly shorter than the energy relaxation timescale ($T1$) [21, **?**]. Unital channels effectively model this rapid decoherence, and are often used to describe the dynamics of qubits in the presence of a classical bath [21].

2.3. Deriving the Quantum Feature Space

The previous grey-box approach to qubit control of [15, 16] used expectations and control pulse amplitudes to train a model, both classical feature spaces. This motivated us to develop a method to deduce the $Q_O D_O Q_O^\dagger$ operators and their parameters from observable expectations. This allowed us to understand the properties of the qubit bath over time. The feature space formed from the parameters of $Q_O D_O Q_O^\dagger$ was hypothesized to be a richer feature space than those used in the previous work. By creating a rich feature space, we could classify noise processes without needing expensive deep learning models.

Substituting Eq. (12) into Eq. (9) gives,

$$\mathbb{E}\{O(T)\}_\rho = \mathrm{Tr}\left[Q_O D_O Q_O^\dagger U_{\mathrm{ctrl}}\rho U_{\mathrm{ctrl}}^\dagger\right] \tag{15}$$

To calculate the mapping between expectations and $Q_O D_O Q_O^\dagger$, one must understand *a priori* the generalised structure of $Q_O D_O Q_O^\dagger$. Recalling the definition of Q_O, we find $Q_O D_O Q_O^\dagger$ is,

$$\begin{bmatrix} \mu_O \cos(2\theta_O) & -e^{2i\psi_O}\mu_O \sin(2\theta_O) \\ -e^{-2i\psi_O}\mu_O \sin(2\theta_O) & -\mu_O \cos(2\theta_O) \end{bmatrix} = \begin{bmatrix} \gamma_O & \alpha_O - \beta_O i \\ \alpha_O + \beta_O i & -\gamma_O \end{bmatrix} \tag{16}$$

with $-1 \le \alpha_O, \beta_O, \gamma_O \le 1$.

Now $U_{\mathrm{ctrl}}\rho U_{\mathrm{ctrl}}^\dagger$ must be Hermitian, with trace one, such that,

$$U_{\mathrm{ctrl}}\rho U_{\mathrm{ctrl}}^\dagger = \begin{bmatrix} a_\rho & b_\rho - c_\rho i \\ b_\rho + c_\rho i & 1 - a_\rho \end{bmatrix} \tag{17}$$

with $0 \le a_\rho, b_\rho, c_\rho \le 1$.

We can now calculate the generalised form of $\mathbb{E}\{O(T)\}_\rho$ in terms of the newly introduced parameters,

$$\mathbb{E}\{O(T)\}_\rho = 2b_\rho \alpha_O + 2c_\rho \beta_O + (2a_\rho - 1)\gamma_O \tag{18}$$

For each observable, there are six initial states, so to find solutions $\alpha_O, \beta_O, \gamma_O$ for each observable, we need to solve an over-determined system of six equations with three unknowns,

$$\begin{bmatrix} 2b_{\rho_{x+}} & 2c_{\rho_{x+}} & (2a_{\rho_{x+}} - 1) \\ 2b_{\rho_{x-}} & 2c_{\rho_{x-}} & (2a_{\rho_{x+}} - 1) \\ \vdots & \vdots & \vdots \\ 2b_{\rho_{z-}} & 2c_{\rho_{z-}} & (2a_{\rho_{z-}} - 1) \end{bmatrix} \begin{bmatrix} \alpha_O \\ \beta_O \\ \gamma_O \end{bmatrix} = \begin{bmatrix} \mathbb{E}\{O\}_{\rho_{x+}} \\ \mathbb{E}\{O\}_{\rho_{x-}} \\ \vdots \\ \mathbb{E}\{O\}_{\rho_{z-}} \end{bmatrix} \tag{19}$$

with $\rho_{x+}, \rho_{x-}, \ldots, \rho_{z-}$ being the standard eigenstates of the Pauli matrices.

The section has also shown how the quantum simulator takes a control sequence and stochastic realisation defined for t timesteps and produces quantum feature space

parameters (α_O, β_O, and γ_O) and observable expectations ($\mathbb{E}\{O(T)\}_\rho$). Properties within the quantum feature space (such as the Euclidean distance) can then be used to estimate the underlying noise model and its parameters. The quantum feature space can also form the input to a simple machine learning algorithm (such as a random forest) or a small neural network, both with nine inputs for the single-qubit case (three parameters for each of the three observables). The output of the machine learning algorithm can be used to classify properties of the noise process, such as its stationarity and type, where the algorithm is trained on labels from the known simulated noise processes. The trained model can then be applied to an unknown noise process from a physical quantum computer to estimate the noise properties and parameters.

3. Experimental Results

3.1. Efficiency of Quantum Feature Space Derivation

To find the best fit solution for Eq. (19), we used the Moore-Penrose inverse [22]. We implemented the Moore-Penrose inverse and methodologies of Sec. 2.3 using *Pytorch* [23] and parallelised calculations using across a GPU. The GPU for all experiments and simulations was an NVIDIA GeForce RTX 3060 with 12GB of memory.

To test and verify the methods of Sec. 2.3 we used ground truth expectations and the corresponding V_O operators from *QDataSet* [24]. A batch of 1000 expectations was used to derive the parameters μ_O, θ_O, and ψ_O, with a total time of 0.52 ± 0.05 ms.

3.2. Quantum Simulation Implementation

Our quantum simulator followed the formalism defined in Sec. 2 and was implemented in *Pytorch* [23]. We noted inefficiencies in the simulator of [24], which led to long execution times, motivating the need for a redesigned simulator to allow frequent and fast experiments. In the redesigned simulator, an overall improvement was using tensor operations whenever possible for the operations presented in Sec. 2.

Our simulator further reduced execution time by computing the unitary at timestep t via left multiplying the unitary at time step $t-1$ by the exponentiated Hamiltonian at time step t. This method was not used in the previous simulator to compute unitaries, and instead, unitaries were computed via recomputing the entire product of required exponentiated Hamiltonians.

A further improvement was that our simulation did not compute the toggled system bath unitary ($U_{\text{SB}}^{\text{tog}}(t)$) for all timesteps; instead, only the final time step toggled system bath unitary was calculated as this was the only unitary required for expectation calculations. By enforcing this, we could exploit the associativity of matrix multiplication and implement a binary tree structure to compute the final unitary, which required $O(\log(N))$ multiplications, where N is the number of time steps.

We benchmarked our simulator and found what required a few days for single qubit simulation in the previous implementation [24] took 10 minutes with the new simulator, giving over a $400\times$ improvement. Greater speed-ups can be achieved if computing at lower precision and or using a GPU with more memory, where both options enable larger batch sizes.

Note, for simulator experiments, we derived the quantum feature space parameters directly and did not calculate expectations as we had access to the $Q_O D_O Q_O^\dagger$ operators. However, when using expectations from a physical quantum computer, one only needs to calculate $U_{\mathrm{ctrl}}(T)\rho U_{\mathrm{ctrl}}^\dagger(T)$, for the final time step T (using the efficient binary tree structure), and then solve Eq. (19), using efficient methods such as the parallelised Moore-Penrose inverse, to find the parameters α_O, β_O, and γ_O.

3.3. Creation of Quantum Feature Space Data

To create the quantum feature space data, we started with noise models and realisation generation methods following that of *QDataSet* [24]. All noise processes acted along the x and z axes, with the noise processes being correlated between the axes. This correlation was achieved by setting the noise values along the z-axis to be the absolute value of the x-axis values (similar to noise profile N6 in *QDataSet*).

Our experiments explored the following noise processes:

- a noise process with a $1/f$ noise PSD (N5 in *QDataSet*)

- a noise process with a $1/f$ noise PSD with a Gaussian-shaped bump in the PSD (N1 in *QDataSet*)

- a Gaussian coloured noise process (N2 in *QDataSet*)

There were six different noise processes in total. The first three were the above noise processes, and the other three were non-stationarity variants of each noise process. To achieve non-stationarity, we multiplied the noise processes by a deterministic triangular time envelope. The envelope was a triangular function with a peak at $T/2$ and a width of T.

The second noise process '$1/f$ + bump' was chosen because it shared similarities with the first noise process ($1/f$). It was hypothesised that these two noise processes would result in parameters close together in the quantum feature space. Conversely, the third process (Gaussian coloured) was chosen because it was hypothesised that it would result in parameters far from the points of the first two noise processes.

Control pulses were applied along the x-axis for all simulations, where the control pulses were approximations of CPMG pulses. To achieve CPMG pulses, we created Gaussian-

shaped pulses of the form

$$f_j(t) = \sum_{n=1}^{n_{max}} A_n e^{-\frac{(t-\tau_n)^2}{2\sigma^2}} \tag{20}$$

where $\sigma = \frac{T}{\lambda M}$, $\lambda \in \mathbb{R}^+$ is the pulse width, T is the total time, M is the number of time steps, $\tau_n = \left(\frac{n-0.5}{n_{max}}\right) T + \delta_\tau$, with $\delta_\tau \in \mathbb{R}$ being used to add jitter to the pulse timing, and A_n is the amplitude of the nth pulse. For all experiments, the number of pulses was $n_{max} = 5$, 1024 discrete time steps were used and ensemble averaging was performed over 2000 realisations of the noise process for a given control pulse sequence.

3.4. Black Box Classification of Bath Through Quantum Feature Space

We conducted a series of simulations to test the ability of the quantum feature space to classify distinct noise processes, where the quantum feature space (Q_O) is the space formed by using the three parameters α_O, β_O, and γ_O from Eq. (16). We first simulated qubit dynamics subject to realisations of the above noise processes with the approximated ideal CPMG pulses. We then simulated a '$1/f$ + bump' process changing the location of its peak compared to earlier noise processes, which emulated an unknown noise process from a physical qubit that an experimentalist would be trying to classify.

While simulating a qubit in the presence of the realisation of an unknown noise process, we used more realistic CPMG pulses; the pulse width was increased, and jitter was added to the peak's timing and value. From the realistic CPMG pulses, we ended up with a cluster of points in the feature space arising from distinct realisations of the jitter. In a black box manner, we identify which noise process characterises the unknown noise process by measuring which *a priori* noise process the cluster of points was closest to in the quantum feature space.

To simulate ideal CPMG pulses, we set $\lambda = \frac{1}{96}$, $\delta_\tau = 0$, $n_{max} = 5$, and $A_n = \pi$. These values were chosen to approximate delta function pulses, shown in the top panel of Fig. 2. For the realistic CPMG pulses we set $\lambda = \frac{1}{24}$, δ_τ was chosen from a uniform random distribution spanning the interval $[-\frac{24T}{M}, \frac{24T}{M}]$, and $A_n = \pi + \epsilon$ where ϵ was drawn from a uniform random distribution spanning the interval $[-\frac{\pi}{5}, \frac{\pi}{5}]$. This is shown in the bottom panel of Fig. 2. Fifty such unique realistic control pulse sequences were generated with ensemble averaging over 2000 noise process realisations for each control pulse, resulting in a cluster of 50 unique points in the quantum feature space.

From the first round of simulations, we calculated the average of the Euclidean distances between the realistic data points and the single data point from the *a priori* noise processes for the feature spaces associated with Q_X, Q_Y, and Q_Z, with the results shown in Table 1. We found that the '$1/f$ + bump' noise process had the smallest total average Euclidean distance across all feature spaces, indicating the stationary '$1/f$ + bump' noise process is likely closest to the unknown noise process.
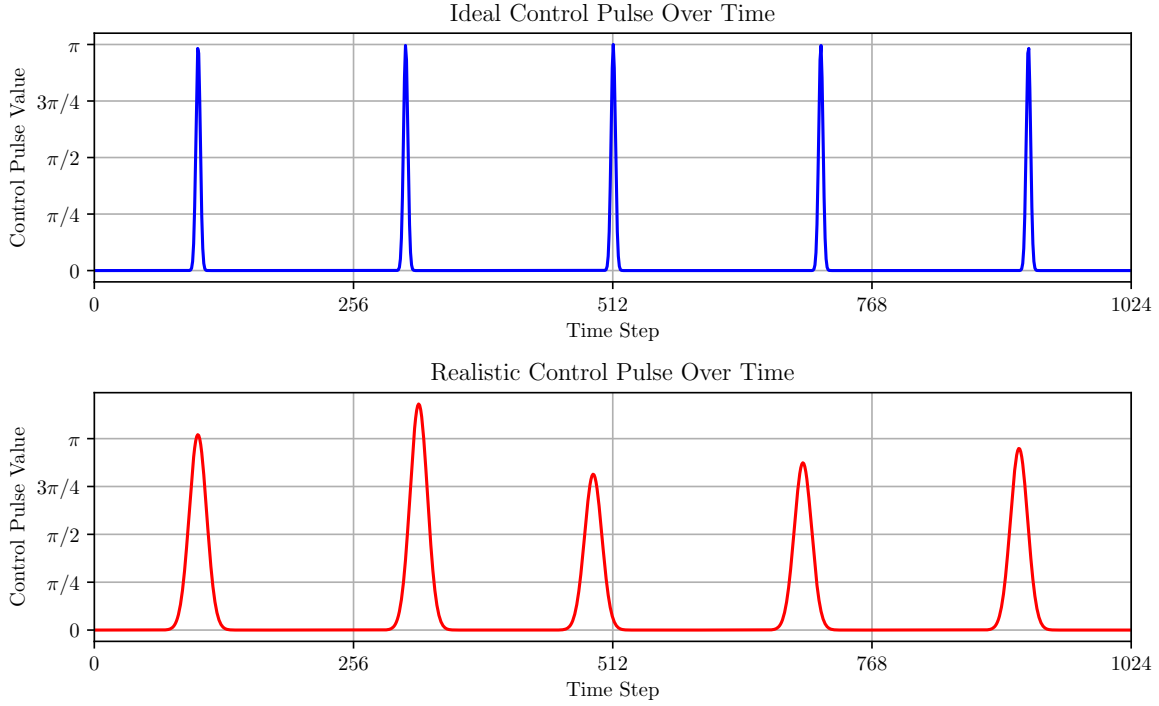
Figure 2: Control pulses used in the simulations. The top row shows the ideal CPMG pulses and the bottom row shows the realistic CPMG pulses.

To refine our classification of the unknown noise process, using the results of the first iteration, we simulated several '$1/f$ + bump' noise profiles, varying the location of the peak in the PSD. Specifically, peaks were positioned at predefined frequency bins, such as the 15th or 30th bin. The result shown in Table 2 indicated that the noise processes with peaks in the 240th and 120th bins were the closest matches, as measured by the average Euclidean distances in the quantum feature space to the unknown process, which peaks at the 200th bin.

It is interesting to note the significantly larger distances between the '$1/f$ + bump' noise processes and the coloured noise processes. This enforces the hypothesis that the quantum feature space encodes the noise process characteristics, as such all the coloured noise processes are significantly further away from the '$1/f$ + bump' noise processes than the '$1/f$ + bump' noise processes are from each other. On the other hand, each noise process has a similar distance metric to its corresponding non-stationary noise process. This indicates that the non-stationary and stationary noise processes result in similar parameters in the quantum feature space, indicating that the quantum feature space is not as sensitive to non-stationarity.

We also observed a relationship between the location of the simulated PSD peak and the average Euclidean distance in the quantum feature space to the unknown process (which has a peak at the 200th bin). Specifically, noise processes with peaks closer to

	$1/f$	$1/f$ (NS)	$1/f$ + bump	$1/f$ + bump (NS)	Coloured	Coloured (NS)
V_x	0.398	**0.368**	0.379	0.381	0.828	0.924
V_y	0.303	0.307	**0.246**	0.269	0.812	0.857
V_z	**0.290**	0.297	0.304	0.293	0.687	0.621
Total	0.991	0.973	**0.929**	0.943	2.326	2.402

Table 1: Average Euclidean distances between realistic data points and the corresponding noise process values in the feature spaces of Q_X, Q_Y, and Q_Z. For each V_O (row), the lowest (best) value is bolded. The total distance is the sum of the distances across all three feature spaces. The overall closest noise process is the '$1/f$ + bump' noise process, with the smallest total distance as bolded. NS indicates non-stationary noise processes.

	15th	30th	60th	120th	240th	480th
V_x	0.367	0.365	0.367	0.322	**0.279**	0.557
V_y	0.241	0.239	0.226	0.153	**0.108**	0.578
V_z	0.296	0.282	0.303	0.292	**0.279**	0.286
Total	0.903	0.885	0.896	0.767	**0.666**	1.422

Table 2: Average Euclidean distances between realistic data points and the corresponding noise process values in the feature spaces of Q_X, Q_Y, and Q_Z. For each V_O (row), the lowest (best) value is bolded. The total distance is the sum of the distances across all three feature spaces. The overall closest noise process is the 240th noise profile, as indicated by the lowest total distance.

the 200th bin, such as the 120th and 240th bin profiles, resulted in smaller distances in the feature space (0.767 and 0.666 respectively). Conversely, peaks further away, like the 15th or 480th bins, corresponded to significantly larger distances (0.903 and 1.422). This correlation demonstrates that the quantum feature space effectively encodes the key characteristics of the noise PSD and that the "distance" between noise processes in terms of their spectral properties (i.e. the location of the peak in the PSD) is meaningfully represented by distance in the quantum feature space. This finding further strengthens the hypothesis that the quantum feature space is a valuable tool for noise spectroscopy.

The results in this section demonstrate that one could simulate a broad class of noise processes to derive quantum features and compare them to quantum features from experimental data with an unknown noise process. Once the general noise process is found, a binary search could be performed to estimate specific parameters of this unknown noise process by minimising distance in the quantum feature space.

3.5. Decision Tree for Noise Characterisation

We then explored the ability of simple ML algorithms to use this quantum feature space. To do this, we generated 600 different noise processes and trained a random forest with K-Fold cross-validation [25, 26]. For the 600 distinct noise processes, 200 processes were $1/f$, 200 were '$1/f$ + bump', and 200 were coloured noise. For each noise process type, half were stationary, and half were non-stationary, i.e. 100 $1/f$ stationary noise processes and 100 $1/f$ non-stationary noise processes. We randomised several parameters between each noise profile to create distinct processes to ensure a diverse and representative dataset. Table 3 summarises the randomised parameters for each noise process and the range of values used. For the $1/f$ noise processes, the exponent (α) was varied, and for the '$1/f$ + bump', the bump location in the frequency domain (μ) was varied alongside α. For coloured noise, the division factor controlling the filter was randomised. For all non-stationary profiles, the peak position of the triangle envelope as a fraction of the total time (T) was randomised.

Noise Profile Type	Parameter	Range/Value
$1/f$	α	[0.7, 1.3]
'$1/f$ + Bump'	μ	[0, 256]
	α	[0.7, 1.3]
Coloured	Division Factor	[2, 16]
Non-Stationary	Peak of deterministic signal	[$0.1T$, $0.9T$]

Table 3: Summary of noise profile characteristics.

To analyse the noise profiles, we used a random forest classifier from the *scikit-learn* library [26]. The classifier was trained on the combined vector components across all three quantum feature spaces, employing a 10-fold cross-validation approach. Each sample was labelled for stationarity and noise type, where two different trees were trained for each classification task. The decision tree classifier for stationarity achieved an average test accuracy of 0.98, and the noise type classifier achieved an average test accuracy of 0.97.

The feature importances for stationarity and noise type classification are shown in Table 4. The feature importance is calculated as the sum of the reduction in the Gini impurity index across all nodes in the tree that use the feature [26]. Interestingly, for both classification tasks, only 3-4 features were needed to explain the majority of the variance in the data, where at least one feature per observable had high importance. This demonstrates how noise process characteristics manifest themselves in the quantum feature space, which may assist in future work to clarify the mapping between a given noise process characteristic and the quantum feature space.

The high accuracy of a simple inexpensive machine learning algorithm, random forest in this case, in both tasks demonstrates the effectiveness of the quantum feature space

Classification Task	α_X	β_X	γ_X	α_Y	β_Y	γ_Y	α_Z	β_Z	γ_Z
Stationarity	0.22	0.08	0.16	0.08	0.15	0.03	0.05	0.08	0.15
Noise Type	0.09	0.14	0.07	0.15	0.13	0.08	0.03	0.03	0.28

Table 4: Feature importances represent the average contributions of the features α, β, and γ for each of the Quantum Feature Spaces Q_X, Q_Y, and Q_Z to the classification task. The feature importances are normalised to sum to 1.

parameters in distinguishing between different noise processes and determining their stationarity. These results further validate our approach and provide a robust method for characterising and classifying noise in quantum systems.

3.6. Properties of the Quantum Feature Space

We sought to understand the mapping between control and noise parameters and the quantum feature space. For these experiments, we explored the impact of widening control pulse widths, which simulated less ideal delta function pulses, the interpolation between noise profiles, and the impact of increasing noise energy.

We first explored the impact of widening control pulse widths on the quantum feature space. The control pulse width was varied by changing the value of λ in Eq. (20). We set $\lambda = \frac{1}{96}, \frac{1}{48}, \frac{1}{24}, \frac{1}{12}, \frac{1}{6}$, and $\frac{1}{3}$. For these simulations, we used the '$1/f$ + bump' with a bump in the PSD at the 200th bin (the unknown noise process from Sec. 3.4). Fig. 3(a) illustrates the impact of widening control pulse widths. The figure shows the interpolation between data points arising from widening control pulses is smooth and well-ordered, providing evidence that the quantum feature space is well-behaved, where it is known that smooth interpolation in a feature space is a highly desirable characteristic [27, 28, 29, 30].

The results in Fig. 3(b) are similar and show a smooth interpolation between the $1/f$ noise process with a bump and the coloured Gaussian noise process. These interpolations were achieved by creating various linear combinations of the noise processes at different ratios, progressively transitioning from one to the other.

We then investigated the impact of increasing the signal energy of the '$1/f$ + bump' and coloured Gaussian noise processes. Signal energy here is defined as,

$$E = \sum_{t=1}^{N} |n_t|^2 \tag{21}$$

where n_t is the noise process value at time step t and N is the total number of time steps. To implement increasing energy, we scaled all values of a given noise realisation (i.e. all n_t) by a constant using the following scale factors: 0.25, 0.5, 0.75, 1.0, 1.25, 1.5, 1.75.

Results for increasing noise strengthen experiments are shown in Fig. 3(c), where increasing colour saturation represents increasing energy. For the coloured noise process and '$1/f$ + bump', as the noise strength increases, all points tend toward the centre of the feature space, where α_O, β_O, and γ_O are all equal to zero. Observe that when α_O, β_O, and $\gamma_O = 0$, $Q_O D_O Q_O^\dagger$ becomes a zero matrix, and looking to Eq. (15), we find that the expectation of the observable is zero. This indicates that as the noise process increases in energy it saturates the system, and as such all information about the noise process and control is lost. Conversely, as the noise strength decreases, points move toward the associated identity in the quantum feature space and therefore result in the system dynamics being dominated by the control pulses.

However, the '$1/f$ + bump' noise process shows a more complex behaviour in Fig. 3(c) when compared to the coloured noise process. The red dots, which represent the '$1/f$ + bump' noise process, rotate around Q_X and Q_Y as the noise strength increases. This rotation is likely due to the spectral bump in the noise profile, which introduces off-diagonal components into the noise operator. In a quantum system under control pulses, such off-diagonal elements can lead to phase shifts or rotations in the operator representation. Essentially, the result shows that the '$1/f$ + bump' noise process does not simply scale the operator uniformly; it alters its orientation in the feature space.

It is interesting to note that for the $1/f$ noise process, the second strongest noise point is closest to the identity (rather than the weakest noise point). One explanation of this phenomenon is the interplay between the noise's rotational effect and its contracting effect (i.e., the tendency to "wash out" information) is nonlinear. As such, at a particular noise level, the destructive interference between the control dynamics and the noise perturbations may nearly cancel out.

For both noise processes, behaviour in the Q_Z feature space is more intuitive; points get closer to the identity as the noise decreases, indicating that the control pulses are dominating system dynamics. Overall this nuanced behaviour seen in these experiments highlights the richness of the quantum feature space and suggests that further study—perhaps through controlled variations or analytical modeling—could provide deeper insight into these dynamics.

4. Conclusion and Future Work

This work has introduced a quantum feature space based on the noise operator formalism. To create this quantum feature space, we extended the noise operator formalism to map experimental measurements directly to system-bath interaction operator parameters. We visualised the quantum feature space, mapping its behaviour to control pulse and noise process parameters. It was found that quantum feature space can be illuminating and used to identify unknown qubit noise processes without making restrictive assumptions and is a promising tool for future noise characterisation.
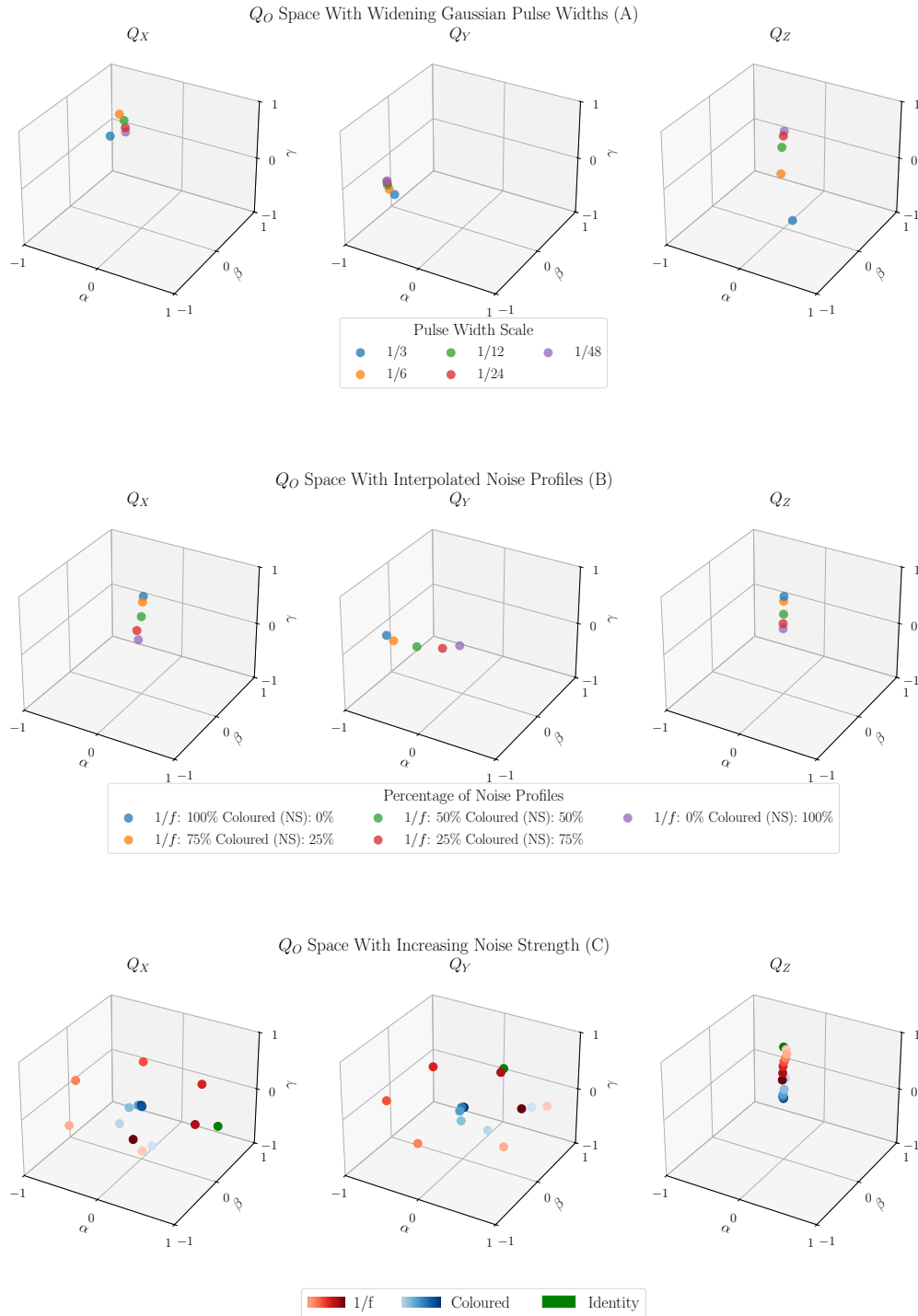
Figure 3: (a) Visualisation of the quantum feature space with widening Gaussian-shaped control pulses, with the fraction indicating the scale factor. (b) Visualisation of the quantum feature space with interpolation between noise processes implemented by utilising a linear combination of the '$1/f$ + bump' and coloured Gaussian noise processes. (c) Visualisation of the quantum parameter space with two different noise processes, '$1/f$ + bump' and coloured Gaussian, with colour saturation representing increasing energy.

Future work could further refine control techniques within the quantum feature space, enhancing the ability to mitigate noise effects. In particular, exploring different types of control pulses and their parameters could provide deeper insights into optimising qubit control for various noise environments. This also includes studying a broader range of noise processes to further validate the developed methodology. Incorporating non-stationary and non-Gaussian noise models further helps us understand the quantum feature space. The methods developed could also be applied and studied in higher-dimensional quantum systems in both simulated and experimental settings.

5. Data and Code Availability

The data and code are available here:
`https://github.com/ChrisWise07/quantum_feature_space`

Acknowledgments

6. References

[1] Sergey Bravyi, Matthias Englbrecht, Robert König, and Nolan Peard. Correcting coherent errors with surface codes. *npj Quantum Information*, 4(1):1–6, 2018.
[2] Lorenza Viola, Emanuel Knill, and Seth Lloyd. Dynamical decoupling of open quantum systems. *Physical Review Letters*, 82(12):2417, 1999.
[3] Christian L Degen, Friedemann Reinhard, and Paola Cappellaro. Quantum sensing. *Reviews of modern physics*, 89(3):035002, 2017.
[4] Jens M Boss, Kevin Chang, Julien Armijo, Kristian Cujia, Tobias Rosskopf, Jerónimo R Maze, and Christian L Degen. One-and two-dimensional nuclear magnetic resonance spectroscopy with a diamond quantum sensor. *Physical review letters*, 116(19):197601, 2016.
[5] Herman Y Carr and Edward M Purcell. Effects of diffusion on free precession in nuclear magnetic resonance experiments. *Physical review*, 94(3):630, 1954.
[6] Saul Meiboom and David Gill. Modified spin-echo method for measuring nuclear relaxation times. *Review of scientific instruments*, 29(8):688–691, 1958.
[7] Gonzalo A Álvarez and Dieter Suter. Measuring the spectrum of colored noise by dynamical decoupling. *Physical review letters*, 107(23):230501, 2011.
[8] Uwe von Lüpke, Félix Beaudoin, Leigh M Norris, Youngkyu Sung, Roni Winik, Jack Y Qiu, Morten Kjaergaard, David Kim, Jonilyn Yoder, Simon Gustavsson, et al. Two-qubit spectroscopy

of spatiotemporally correlated quantum noise in superconducting qubits. *PRX Quantum*, 1(1):010305, 2020.

[9] Won Kyu Calvin Sun and Paola Cappellaro. Self-consistent noise characterization of quantum devices. *Physical Review B*, 106(15):155413, 2022.

[10] David F Wise, John JL Morton, and Siddharth Dhomkar. Using deep learning to understand and mitigate the qubit noise environment. *PRX Quantum*, 2(1):010316, 2021.

[11] Stefano Martina, Stefano Gherardini, and Filippo Caruso. Machine learning classification of non-markovian noise disturbing quantum dynamics. *Physica Scripta*, 98(3):035104, 2023.

[12] Alessandro Baroni, Joseph Carlson, Rajan Gupta, Andy CY Li, Gabriel N Perdue, and Alessandro Roggero. Nuclear two point correlation functions on a quantum computer. *Physical Review D*, 105(7):074503, 2022.

[13] Stefano Martina, Santiago Hernández-Gómez, Stefano Gherardini, Filippo Caruso, and Nicole Fabbri. Deep learning enhanced noise spectroscopy of a spin qubit environment. *Machine Learning: Science and Technology*, 4(2):02LT01, 2023.

[14] Arian Vezvaee, Nanako Shitara, Shuo Sun, and Andrés Montoya-Castillo. Fourier transform noise spectroscopy. *npj Quantum Information*, 10(1):52, 2024.

[15] Akram Youssry, Gerardo A Paz-Silva, and Christopher Ferrie. Characterization and control of open quantum systems beyond quantum noise spectroscopy. *npj Quantum Information*, 6(1):95, 2020.

[16] Akram Youssry and Hendra I Nurdin. Multi-axis control of a qubit in the presence of unknown non-markovian quantum noise. *Quantum Science and Technology*, 8(1):015018, 2022.

[17] Amanda E Seedhouse, Nard Dumoulin Stuyck, Santiago Serrano, Will Gilbert, Jonathan Yue Huang, Fay E Hudson, Kohei M Itoh, Arne Laucht, Wee Han Lim, Chih Hwan Yang, et al. Wavelet correlation noise analysis for qubit operation variable time series. *Scientific Reports*, 15(1):11065, 2025.

[18] Kiyoto Nakamura and Joachim Ankerhold. Gate operations for superconducting qubits and non-markovianity. *Physical Review Research*, 6(3):033215, 2024.

[19] Youngkyu Sung, Félix Beaudoin, Leigh M Norris, Fei Yan, David K Kim, Jack Y Qiu, Uwe von Lüpke, Jonilyn L Yoder, Terry P Orlando, Simon Gustavsson, et al. Non-gaussian noise spectroscopy with a superconducting qubit sensor. *Nature communications*, 10(1):3715, 2019.

[20] Gerardo A Paz-Silva, Leigh M Norris, and Lorenza Viola. Multiqubit spectroscopy of gaussian quantum noise. *Physical review a*, 95(2):022121, 2017.

[21] Michael A Nielsen and Isaac Chuang. Quantum computation and quantum information, 2002.

[22] Roger Penrose. A generalized inverse for matrices. In *Mathematical proceedings of the Cambridge philosophical society*, volume 51, pages 406–413. Cambridge University Press, 1955.

[23] Adam Paszke, Sam Gross, Francisco Massa, Adam Lerer, James Bradbury, Gregory Chanan, Trevor Killeen, Zeming Lin, Natalia Gimelshein, Luca Antiga, et al. Pytorch: An imperative style, high-performance deep learning library. *Advances in neural information processing systems*, 32, 2019.

[24] Elija Perrier, Akram Youssry, and Chris Ferrie. Qdataset, quantum datasets for machine learning. *Scientific Data*, 9(1):582, 2022.

[25] Gareth James. An introduction to statistical learning, 2013.

[26] F. Pedregosa, G. Varoquaux, A. Gramfort, V. Michel, B. Thirion, O. Grisel, M. Blondel, P. Prettenhofer, R. Weiss, V. Dubourg, J. Vanderplas, A. Passos, D. Cournapeau, M. Brucher, M. Perrot, and E. Duchesnay. Scikit-learn: Machine learning in Python. *Journal of Machine Learning Research*, 12:2825–2830, 2011.

[27] Yoshua Bengio, Aaron Courville, and Pascal Vincent. Representation learning: A review and new perspectives. *IEEE transactions on pattern analysis and machine intelligence*, 35(8):1798–1828, 2013.

[28] Alec Radford, Luke Metz, and Soumith Chintala. Unsupervised representation learning with deep convolutional generative adversarial networks. *arXiv preprint arXiv:1511.06434*, 2015.

[29] Jiayi Guo, Xingqian Xu, Yifan Pu, Zanlin Ni, Chaofei Wang, Manushree Vasu, Shiji Song, Gao Huang, and Humphrey Shi. Smooth diffusion: Crafting smooth latent spaces in diffusion models. In *Proceedings of the IEEE/CVF Conference on Computer Vision and Pattern Recognition*, pages 7548–7558, 2024.

[30] Irina Higgins, Loic Matthey, Arka Pal, Christopher Burgess, Xavier Glorot, Matthew Botvinick, Shakir Mohamed, and Alexander Lerchner. beta-vae: Learning basic visual concepts with a constrained variational framework. In *International conference on learning representations*, 2017.